The Astrophysical Journal, 961:149 (15pp), 2024 February 1 https://doi.org/10.3847/1538-4357/ad11d3

"Tidal Peeling Events": Low-eccentricity Tidal Disruption of a Star by a Stellar-mass Black Hole

Chengcheng Xin[1], Zoltán Haiman[1,2], Rosalba Perna[3,4], Yihan Wang[5,6], and Taeho Ryu[7,8]
[1] Columbia University, Department of Astronomy, 550 West 120th Street, New York, NY 10027, USA; cx2204@columbia.edu
[2] Columbia University, Department of Physics, 550 West 120th Street, New York, NY 10027, USA
[3] Department of Physics and Astronomy, Stony Brook University, Stony Brook, NY 11794-3800, USA
[4] Center for Computational Astrophysics, Flatiron Institute, New York, NY 10010, USA
[5] Nevada Center for Astrophysics, University of Nevada, 4505 S. Maryland Parkway, Las Vegas, NV 89154-4002, USA
[6] Department of Physics and Astronomy, University of Nevada, 4505 S. Maryland Parkway, Las Vegas, NV 89154-4002, USA
[7] Max Planck Institute for Astrophysics, Karl-Schwarzschild-Strasse 1, D-85748 Garching, Germany
[8] Physics and Astronomy Department, Johns Hopkins University, Baltimore, MD 21218, USA
Received 2023 March 27; revised 2023 November 29; accepted 2023 November 30; published 2024 January 22

Abstract

Close encounters between stellar-mass black holes (BHs) and stars occur frequently in dense star clusters and in the disks of active galactic nuclei. Recent studies have shown that in highly eccentric close encounters, the star can be tidally disrupted by the BH in a microtidal disruption event (microTDE), resulting in rapid mass accretion and possibly bright electromagnetic signatures. Here we consider a scenario in which the star might approach the stellar-mass BH in a gradual, nearly circular inspiral, under the influence of dynamical friction in a circum-binary gas disk or three-body interactions in a star cluster. We perform hydrodynamics simulations of this scenario using the smoothed particle hydrodynamics code PHANTOM. We find that under certain circumstances (for initial eccentricity $e_0 \gtrsim 0.4$ and penetration factor $\beta = 1$, or $e_0 < 0.4$ and $\beta \lesssim 0.67$), the mass of the star is slowly stripped away by the BH. We call this gradual tidal disruption a "tidal-peeling event." Additionally, we discover that some low-eccentricity microTDEs ($e_0 < 0.4$ and $\beta = 1$) are a new form of fast luminous transients similar to parabolic microTDEs. Depending on the initial distance and eccentricity of the encounter, these low-eccentricity microTDEs might exhibit significant accretion rates and orbital evolution distinct from those of a typical (eccentric) microTDE.

Unified Astronomy Thesaurus concepts: High energy astrophysics (739); Active galactic nuclei (16); Tidal disruption (1696)

1. Introduction

Stars and their compact remnants, which include stellar-mass black holes (BHs), are expected to be abundant in dense stellar clusters of all kinds (Mackey et al. 2007; Strader et al. 2012), and they can also be found in the disks of active galactic nuclei (AGNs). Dynamical interactions between compact objects and stars in clusters are frequently expected (Rodriguez et al. 2016; Kremer et al. 2018). As a result, stars in a cluster will inevitably undergo close encounters with stellar-mass BHs. These close encounters between stars and BHs, which are of particular interest here, can lead to binary formation or to tidal disruption of the star by the BH, called a microtidal disruption event (microTDE; Perets et al. 2016).

Stars and stellar-mass BHs found in an AGN disk are likely the result of two mechanisms: (i) capture from the nuclear star cluster (Artymowicz et al. 1993), which consists mostly of massive stars (e.g., O- and B-type stars with masses $\gtrsim$2–15 $M_\odot$): these stars' orbits will eventually align with the AGN disk after a number of crossings of the disk (Yang et al. 2020), and (ii) in situ formation: gravitational instabilities in the outer parts of the disk trigger star formation (Kolykhalov & Syunyaev 1980; Goodman 2003; Dittmann & Miller 2020), and those stars, as well as their remnant compact objects, remain embedded in the disk. The unusual disk environment causes stars to accrete and grow in mass much more rapidly than elsewhere in the interstellar medium, changing the stars' structure, allowing them to reach much higher masses, and making BH remnants a more common outcome upon their death (Cantiello et al. 2021; Dittmann et al. 2021; Jermyn et al. 2021). Once trapped in the AGN disk, BHs can go through radial migration and undergo close encounters with stars or compact objects, which has been shown in both analytical studies (e.g., Tagawa et al. 2020; DeLaurentiis et al. 2023), and hydrodynamics simulations (Li et al. 2023; Rowan et al. 2023a, 2023b; Whitehead et al. 2023) to result in the formation of bound binaries. These binaries can be both retrograde and prograde and also both circular and eccentric, depending on the impact parameter of the encounter. Therefore, microTDEs can also occur in AGN disks, in addition to the stellar cluster environment.

MicroTDEs are expected to be ultraluminous events, and their expected accretion rates and electromagnetic (EM) features have recently begun to be investigated in more detail via smoothed particle hydrodynamics (SPH) simulations (Lopez et al. 2019; Kremer et al. 2021; Wang et al. 2021; Kremer et al. 2022; Ryu et al. 2022) and moving-mesh simulations (Ryu et al. 2023). Existing studies have performed numerical experiments to investigate nearly parabolic encounters with eccentricity $e \sim 1$. Kremer et al. (2022) recently presented a variety of hydrodynamics simulations of typical microTDEs with parabolic orbits to show that stars in a vacuum can experience different degrees of tidal disruption depending on pericenter distance and stellar mass, while the peak luminosity of the EM emission might be super-Eddington

when the pericenter distance is within $\sim 2\ R_t$, where $R_t = (M_{\rm BH}/M_{\rm s})^{1/3} R_{\rm s}$ is the order-of-magnitude estimate of the tidal radius for a star with mass $M_{\rm s}$ and radius $R_{\rm s}$ disrupted by a BH with mass $M_{\rm BH}$.

On the other hand, low-eccentricity microTDEs in compact orbits are of particular interest in this paper for the following reasons. First, observational work has suggested that binaries in clusters have lower eccentricity as they become more compact (Meibom & Mathieu 2005; Hwang et al. 2022). The 3D hydrodynamics simulations by Ryu et al. (2023) further suggest that three-body interactions in clusters such as encounters between binary stars and stellar-mass BHs can also lead to eventual close interactions between one star in the original binary and the BH, where, in some cases, a low-eccentricity microTDE in a close orbit can form if the star becomes bound to the BH. Additionally, star–BH binaries in an AGN disk can become tightly bound due to external torques exerted by the dynamical friction of the AGN disk gas. Hydrodynamics simulations have shown that a circum-binary disk tends to shrink the orbit of the binary within an AGN disk for wide binary separations[9] (Kaaz et al. 2021; Li et al. 2021; Dempsey et al. 2022; Li & Lai 2022), and the binary orbit in the circum-binary disk can be driven to either a circular orbit with $e \to 0$ or else to an eccentric orbit with $e \to 0.45$, depending on the initial eccentricity (Muñoz et al. 2019; D'Orazio & Duffell 2021; Zrake et al. 2021; Siwek et al. 2023), although these latter numerical studies focus on isolated binary BHs.

As demonstrated by this work, low-eccentricity microTDEs can look like a fast ultraluminous transient, such as a parabolic microTDE, where the star's mass is removed rapidly within one or two orbits. However, the star might also experience gradual stripping of mass over many orbital times, analogous, but not limited to, the following events: (i) the extreme mass-ratio inspiral (EMRI) of a white dwarf (WD) and an intermediate-mass black hole (IMBH), in which the WD loses mass periodically during the inspiral (Zalamea et al. 2010; Chen et al. 2022); (ii) EMRI with a supermassive black hole (SMBH) and a main-sequence (MS) star, where mass loss occurs over many orbital times through the L2 Lagrangian point (Linial & Sari 2017); and (iii) quasiperiodic eruptions due to two adjacent stellar EMRIs around an SMBH (Metzger et al. 2022). This makes low-eccentricity microTDEs an origin to a unique scenario that we refer to as "tidal-peeling events" (TPEs), due to the gradual peeling of mass that the star could experience.

The configurations of low-eccentricity, compact BH–star binary encounters can also be regarded as similar to, or extreme cases of, a massive stellar binary's post–common-envelope evolution (e.g., Taam & Sandquist 2000, with more compact circum-binary gas), mass transfer in ultracompact stellar binaries (e.g., Iben & Tutukov 1984), or X-ray binaries (e.g., Van Haaften et al. 2012).

In this paper, we numerically model the general case of TPEs with SPH simulations using PHANTOM, without including low-density background gas such as in an AGN disk. We focus on exploring the BH mass accretion rate and orbital evolution in TPEs under different assumptions for the initial mass of the star, eccentricity, and pericenter distance of the encounter.

[9] Note however that Li et al. (2021) and Dempsey et al. (2022) suggest that as a binary's semimajor axis (SMA) becomes small relative to the Hill radius, the typical evolution of binary orbits within AGN disks can shift from shrinking to expanding.

We organize this paper as follows. We describe our simulation models, analysis method, and a resolution study in Sections 2, 3, and 4, respectively. In Section 5, we show the morphological evolution of the TPEs. Section 6 illustrates our prediction for the EM signatures of TPEs, based on the computation of the BH mass accretion rates, stellar mass loss via tidal interactions, and orbital evolution of the remnant. In Section 7, we explore the effect of having more massive stars undergoing TPEs. Finally, we discuss some implications of our results in Section 8, and we summarize our conclusions in Section 9.

2. Simulation Methods

We perform SPH simulations of TPEs of stars by a 10 $M_\odot$ BH using PHANTOM (Price et al. 2018). We run simulations for (four stellar masses) × (four eccentricities) × (six penetration factors) = 96 models in total, where the penetration factor β is defined as the ratio between the tidal radius and the pericenter distance, or R_t/r_p. We fix the BH mass in all the simulation models at $M_{\rm BH} = 10\ M_\odot$. We consider MS stars with four different masses, $M_{\rm s} = 1$, 5, 10, and 15 $M_\odot$, and investigate the dependence of the initial eccentricities of outcomes by considering $e_0 = 0$, 0.2, 0.4, and 0.6. We begin all simulations by placing the star at the apocenter of the orbit. Finally, we consider penetration factors $\beta = R_t/r_p = 1$, 0.67, 0.5, 0.4, 0.33, and 0.25, which correspond to pericenter distances $r_p = 1$, 1.5, 2, 2.5, 3, and 4 times the tidal radii. Recall that our definition of tidal radius, $R_t = (M_{\rm BH}/M_{\rm s})^{1/3} R_{\rm s}$, is used for all stars of all masses. However, in practice, this definition is only physically applicable if $M_s \ll M_{\rm BH}$, and it needs to be corrected for larger stellar masses. For example, one could define a physically motivated new R_t by requiring the separation a between the BH and the star to be equal to the average size $\bar{r}_L$ of the spherical Roche lobe (Eggleton 1983). For the mass ratios considered above, $\bar{r}_L$ varies in the range $\sim$(0.2–0.4) a, where a is the orbital separation. However, we chose to use the conventional definition for R_t in order to parameterize all of the pericenter distances in the same units across all simulations models. This choice is intuitive because our simulations showcase very close encounters in which the parameter space for r_p ranges from a few tidal radii to almost direct collisions. Additionally, in the (two) models where $M_s \geqslant 10\ M_\odot$ and $\beta = 1$, the stellar radius R_s becomes comparable to ($M_s = 10\ M_\odot$) or larger than ($M_s = 15\ M_\odot$) r_p. Hence in these cases we essentially perform common-envelope simulations. We chose to keep these models for illustration, i.e., so that we sample a consistent parameter space for stars of all masses. For simplicity, we also introduce the letter $\mathcal{M}(M_{\rm s}, e_0, \beta)$ to denote any specific model, where $M_{\rm s}$ is given in units of $M_\odot$.

We first use the 1D stellar evolution code MESA (Paxton et al. 2019) to generate the profile of each MS star with a core H fraction of 0.5, where we assume solar abundances for composition, hydrogen and metal mass fractions $X = 0.74$ and $Z = 0.02$, respectively (helium mass fraction $Y = 1 - X - Z$), and mean molecular weight $\mu \sim 0.59$ (fully ionized gas). For the stellar masses that we consider, MESA uses the OPAL and HELM tables for the equation of state (Paxton et al. 2019), which we adopt in the TPE simulations. We then take the density and internal energy profile of MESA MS stars to start the simulations in PHANTOM. We first map the 1D MESA model onto our 3D SPH grid and relax it for a few stellar dynamical times ($t_{\rm dyn} = \sqrt{R_s^3/GM_s}$) until it reaches hydrostatic

equilibrium. $t_{\rm dyn}$ is typically one to a few hours depending on the mass and radius of the star.

In the TPE simulations with PHANTOM, we use artificial viscosity varying between $a^{\rm AV}{}_{\rm min} = 0.1$ and $a^{\rm AV}{}_{\rm max} = 1$. This is the typical range for $a^{\rm AV}$ to evolve, which contributes to shock capture (e.g., Coughlin et al. 2017). We adopt an equation of state that includes radiation pressure assuming instantaneous local thermodynamic equilibrium. This assumption is valid because the gas in our simulations is expected to be optically thick. We employ 10^5 SPH particles in each simulation, which is justified in Section 4, and each simulation uses up to 6000 CPU hours on an Intel Xeon Gold 6226 2.9 Ghz processor. For this resolution (10^5 SPH particles), we have adopted 100 r_g as the accretion radius for the BH. This radius is sufficiently small to capture the physics of the accretion process accurately in the SPH simulations, while also being large enough to maintain CPU efficiency. Regarded as the softening length of the BH, 100 r_g is the shortest (initial) softening length among all particles in all of our models, where $r_g = GM_{\rm BH}/c^2$. If an SPH particle falls within the "accretion" radius, $r_{\rm acc} = 100$ r_g, it is accreted onto the BH. The particles are removed from the simulation once accreted by the BH; the removed mass is added to the mass of the sink particle.

3. Analysis

In this study, we focus on some key physical quantities, such as the amount of mass lost in the TPEs and the accretion rate, directly measured from our simulation output. Also, we investigate their dependence on different initial conditions: the mass of the star (M_s), the initial eccentricity (e_0), and the penetration parameter (β) that is inversely proportional to the initial pericenter distance.

First, we measure the mass accretion onto the BH, $M_{\rm acc}$, by evaluating the mass accreted onto the sink particle representing the BH. The BH accretion rate $\dot{M}_{\rm BH}$ is computed as the finite difference of $M_{\rm acc}$ divided by the time difference (∼0.4 hr) between two adjacent outputs of the simulation.

In a TPE, the star's mass is slowly stripped by the BH, which leads to the star being partially or totally disrupted. In past studies of tidal disruption events (TDEs) or microTDEs using numerical simulations (e.g., Mainetti et al. 2017; Kremer et al. 2022), the mass bound to the star or BH is usually computed using an iterative process, as described in Lombardi et al. (2006). However, we find this iterative method to be too expensive to perform for all 96 simulation models. Alternatively, we define the mass of the stellar remnant ($M_{\rm rem}$) as the total mass of particles within the initial radius of the star (measured from the densest point in the star). We use the center of mass of this remnant to compute the orbital evolution of the disrupted star. The center of mass offers a good approximation for computing the dynamical interaction between the BH and the remnant, specifically for the stellar core that survives for many orbits of tidal peeling. We find by visual inspection that the center of mass of the remnant remains very close to the center of the spherical region making up $M_{\rm rem}$ throughout our simulations. On the other hand, in microTDEs where the star is significantly deformed and rapidly and totally disrupted, it is not meaningful to investigate the orbital properties. Later in this section, we discuss how we use the center of mass of $M_{\rm rem}$ to obtain the orbital evolution in the TPEs.

In addition to the stellar material lost to $M_{\rm acc}$, the star can also lose mass to the surroundings when the stellar material is unbound during the disruptions. We measure the fraction of total mass removed from the star, $f_{\rm rm}$. The mass removed consists of mass accreted by the BH ($M_{\rm acc}$) and mass ejected (total stellar mass minus remnant mass; $M_{\rm s} - M_{\rm rem}$). Note that the mass removed from the star includes the mass unbound to the remnant, but bound and not yet accreted by the BH. So $f_{\rm rm} = (M_{\rm s} - M_{\rm rem} + M_{\rm acc})/M_s$.

The orbital features of the stellar remnant can be described by the evolution of the orbital separation (r), SMA (a), and eccentricity (e) over time. We define r to be the distance between the particle of the center of mass of the stellar remnant ($M_{\rm rem}$), which is typically near the core of the star, and the position of the sink particle (BH). The location of the center of mass takes into account any small deviations that could occur due to oscillations of the star during the disruption. We adopt a generic method to calculate the SMA and the eccentricity using the specific energy and specific angular momentum of the binary, adapted from the calculations in Muñoz et al. (2019). Here the equations of motion of the binary are evaluated with the external gravitational and accretional forces. Note these calculations are applicable to binaries with moderate mass loss, while in some of our simulations the star can lose a considerable amount of mass. Therefore, we check that the distribution of the SMAs and eccentricities for all fluid elements are well represented by the SMA and eccentricity of the remnant's center of mass in models with no total disruption. In Section 6, we evaluate the evolution of a and e, as well as their change per each orbit around the BH.

4. Resolution Tests of the Initial Stellar Profile

A typical choice for resolutions of hydrodynamics simulations of TDEs or microTDEs is $N \sim 10^5$ particles (e.g., Mainetti et al. 2017; Kremer et al. 2022). We performed resolution tests to determine whether or not a higher resolution is needed, by using PHANTOM to model the initial stellar profile using different numbers of SPH particles: $N = 10^5$, 2×10^5, 4×10^5, 8×10^5, and 10^6. In particular, we compare the radial density profiles of a fully relaxed 1 $M_\odot$ star with the numbers of SPH particles given above in Figure 1. The gray region shows where the initial profile varies the most, which occurs at the surface of the star. We find that different resolutions only cause the density to fluctuate by ∼0.01%, which only takes place in fewer than 1% of the SPH particles by mass and $\lesssim 0.2\ R_\odot$ by radius. Overall, the density profiles for resolutions from $N = 10^5$ to $N = 10^6$ particles show excellent agreement. Therefore, we run all TPE simulations, starting from their stellar profiles, $N = 10^5$ particles. As a comparison, we also depict a polytropic star with $\gamma = 4/3$ of the same mass using a purple dashed line.

Next, we demonstrate that the evolution of the mass accreted by the BH, or $M_{\rm acc}$, does not significantly vary with the number of SPH particles. Figure 2 shows $M_{\rm acc}$ versus time for model $\mathcal{M}(1, 0, 1)$, for different N values varying from 10^5 to 10^6, and demonstrates that $M_{{\rm acc},N}$ varies by no more than ∼0.1%. We also find that the SMA of the remnant, while surviving during the first orbit, varies by no more than 0.1% for different N values. We chose model $\mathcal{M}(1, 0, 1)$ for the convergence tests because this is one of the most extreme cases, which requires the highest resolution.

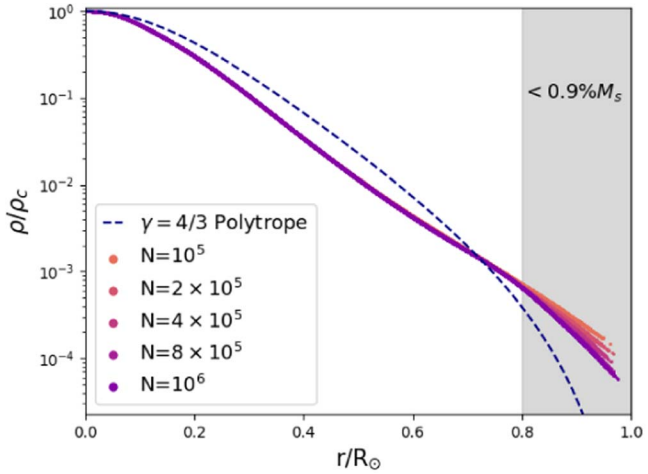

Figure 1. The radial density profile of a fully relaxed 1 $M_\odot$ star in PHANTOM, using $N = 10^5$, 2×10^5, 4×10^5, 8×10^5, 10^6 SPH particles. The density is normalized to the core density ρ_c. Different resolutions yield converging initial density profiles for the star, despite a small surface layer ($R > 0.8\ R_\odot$; gray region), containing $\lesssim$0.9% of stellar mass. This justifies our choice to use $N = 10^5$ particles throughout the simulations. As a sanity check, we overlay the analytical solution of 4/3 polytrope (purple dashed line).

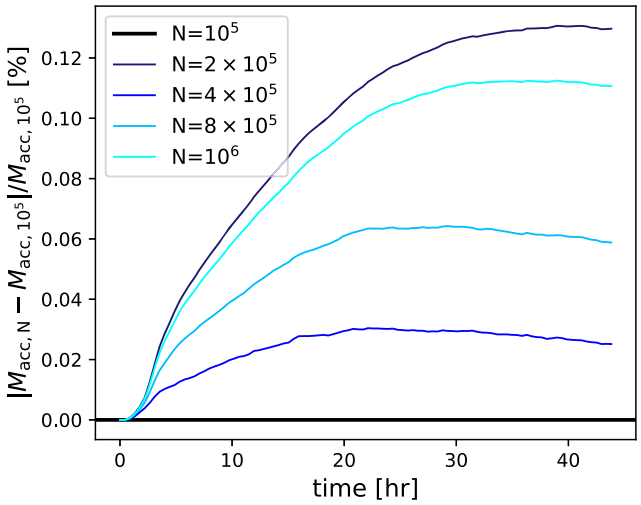

Figure 2. Relative mass accreted onto the BH in simulation model $\mathcal{M}(1, 0, 1)$ for different resolutions, using $N = 10^5$, 2×10^5, 4×10^5, 8×10^5, and 10^6 SPH particles.

5. Morphology of a TPE

The stars in our simulations encounter the BH in low-eccentricity ($e = 0$–0.6) and ultracompact ($\beta = 0.25$–1) orbits. Depending on the initial conditions, the mass of the star can be rapidly stripped (i.e., a TDE) or slowly peeled by the BH, and stellar material is lost on the timescale of many orbital periods (i.e., a TPE). In general, novel morphological evolution is seen in low-eccentricity microTDEs, especially those seen in TDEs. In particular, we observe (1) gradual tidal stripping and the formation of spirals, (2) possible debris–star interactions, and (3) efficient circularization of debris into an accretion disk. Each of these is demonstrated in the following examples.

Figure 3 shows the typical morphology of a TPE, where the column density of the gas particles is shown in the color bar and the BH is represented by the green dot. In this example (model $\mathcal{M}(1, 0.4, 1)$; recall the definition in Section 3), the 1 $M_\odot$ star on an eccentric orbit with $\beta = 1$ is "peeled" due to the tidal influence of the BH, which continues for four orbital times before the star is totally disrupted (approximately during the fourth orbit). The snapshots are taken at $t = 0$, 4.9, 12.0, 18.2, 23.5, and 36.3 hr since the onset of the simulation, where the orbital period is $P \approx 5.7$ hr. Some stellar debris circularize and form an accretion disk around the BH, while some become unbound and are ejected into infinity, including mass lost through the "L3" point; we show the initial equipotential surface of the binary in each panel. This can be more clearly seen in Figure 4, which shows an edge-on view of Figure 3. The disk is initially smaller than the pericenter distance of the orbit for a short period before it inflates and puffs up later on due to radiation pressure and shock heating, similar to the findings of Wang et al. (2021).

Generally, tidal peeling is more violent for smaller orbital separations. All of our TPE simulations result in super-Eddington BH accretion rates. However, a significant fraction of the star being tidally disrupted, leaving most of the dense stellar material around the BH, results in a large optical depth that likely will delay and dim the EM emission from the TPE. In reality, the luminosity could be modulated by several mechanisms such as jet emission or wind outflow from the accretion disk, which are not included in this study. Additionally, in some configurations, such as $\mathcal{M}(1, 0.6, 0.67)$ in Figure 5, the star intersects with its own tidal streams periodically, which will form a shock front that further modifies the luminosity from the TPE. In this model, the remnant remains intact for many orbits. In the second panel, the star encounters the tail of its own stream formed in the last orbit, leaving behind a hot plume near the star as seen in the last panel. Although these phenomena cannot be resolved in our simulations, in the following sections, we will qualitatively discuss their implications for the overall EM signature of the TPEs in addition to the accretion rates that we measure directly from the simulations.

Finally, TPEs from the interaction of BHs with more massive stars are considered since stars near the Galactic center (Genzel et al. 2003; Levin 2003; Paumard et al. 2006) and those formed in an AGN disk (Levin 2003; Goodman & Tan 2004) are also thought to be preferentially massive, sometimes even much more massive than the stars considered in our simulation, and they offer morphologies different from TPEs with a solar-like star. In Figure 6, we demonstrate a TPE between a 5 $M_\odot$ star and a BH in a circular orbit with an initial separation of one tidal radius. The surface of this star is almost in contact with the BH, $a = r_p \approx 1.3\ R_s$. Compared to a solar-like star in the same initial orbit, a more massive star experiences more rapid tidal peeling. As a result, the spirals formed from the disrupted material are more closely packed, compared to those in Figure 3. The snapshots of the TPE are taken at $t = 0$, 0.88, 1.77, 2.66, 3.54, and 4.43 hr, and this TPE model has an orbital time $P \approx 1$ hr. The massive star is totally disrupted within the first orbit, and the stellar material eventually circularizes into a smooth disk.

6. Accretion Rate and Orbital Evolution of TPEs

6.1. Overview Using Two Examples

Figure 7 demonstrates six key features of mildly eccentric TPEs for the case of the 10 $M_\odot$ BH and the 1 $M_\odot$ star. This figure presents two models: $\mathcal{M}(1, 0.4, 1)$ (left) with an initial eccentricity (e_0) of 0.4 and initial pericenter distance $r_p/R_t = 1$ ($\beta = 1$), and $\mathcal{M}(1, 0.6, 0.67)$ (right), which is a more eccentric

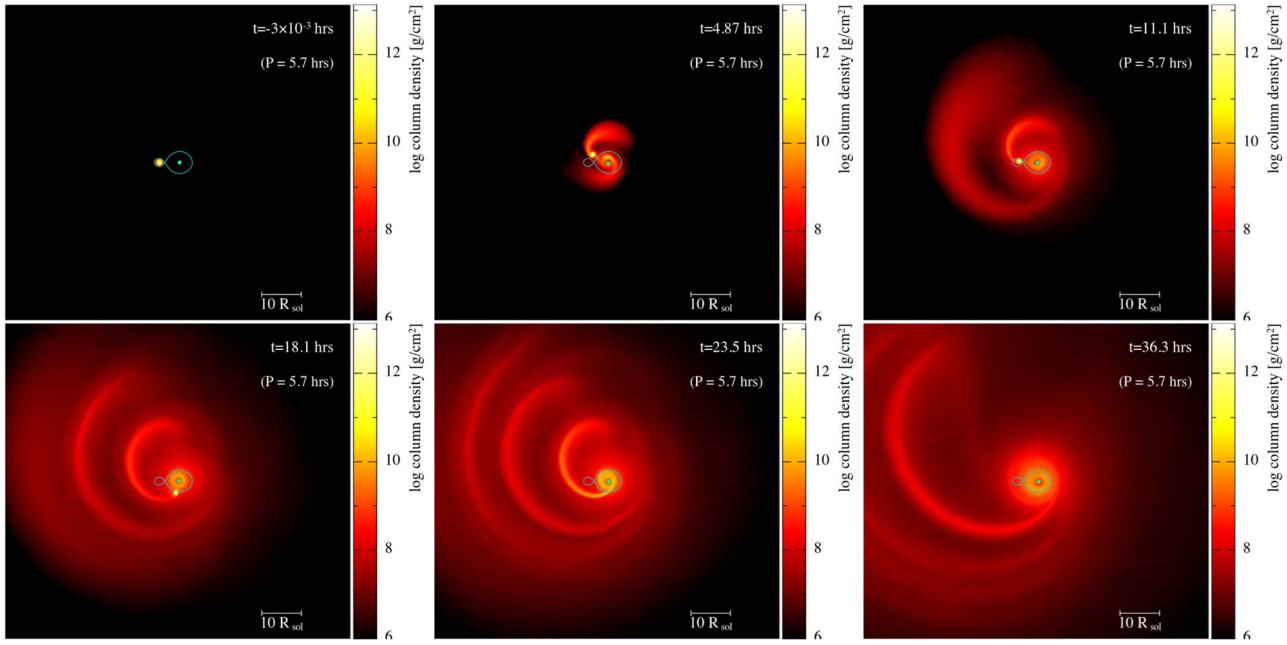

Figure 3. $\mathcal{M}(1, 0.4, 1)$: tidal-peeling morphology of a 1 $M_\odot$ star and a 10 $M_\odot$ BH, where the orbit is initially a low-eccentricity inspiral ($e_0 = 0.4$), and the pericenter distance between star and BH is one tidal radius ($r_p = 2.2\ R_\odot$ and $\beta = 1$). The color bar shows the projection of the log-scale column density in the x–y plane. We overlay the initial equipotential surface of the binary to show that the stellar material fills up the Roche Lobe around the BH, and the star loses mass through the Lagrangian points. The initial orbital period is quoted in parentheses , specifically, $P \approx 5.7$ hr in this model. We show six time frames of the event that demonstrate the tidal "peeling" process, until the star is completely disrupted by the BH. The star orbits around the BH and passes through the pericenter four times until it is torn apart by the BH.

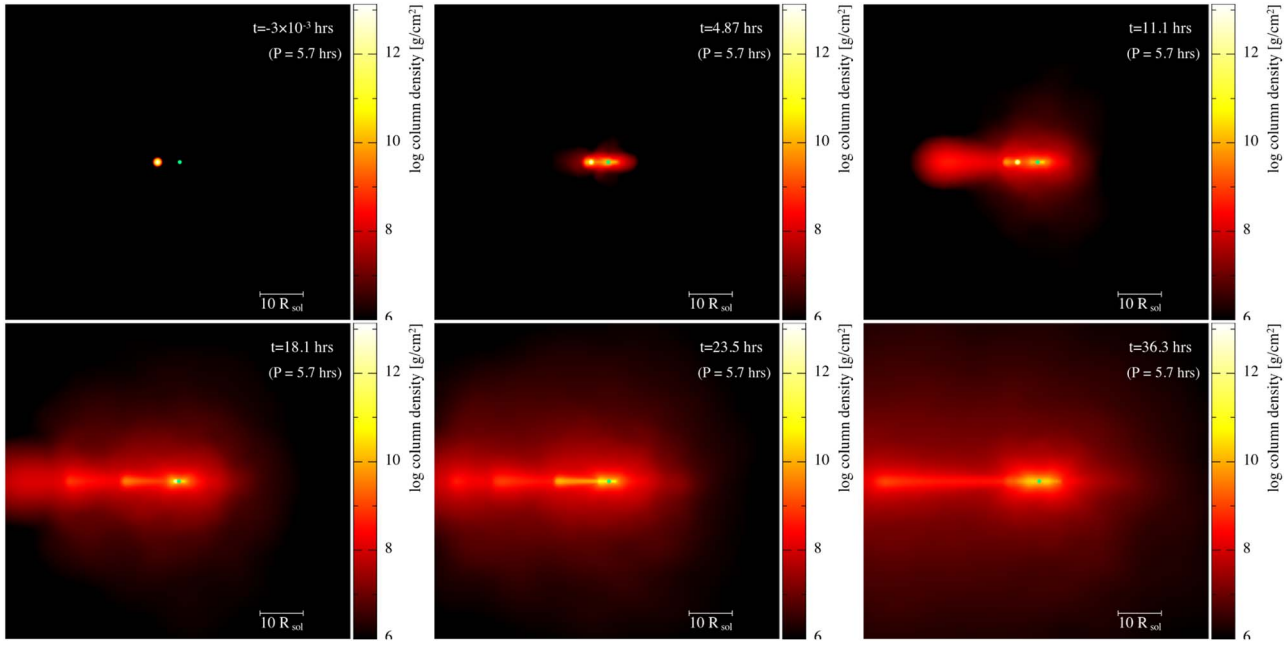

Figure 4. $\mathcal{M}(1, 0.4, 1)$: same snapshots of the simulation as in Figure 3 but this time in the x–z plane, or edge-on view of the orbit and the accretion disk.

and less compact model with $e_0 = 0.6$ and $r_p/R_t = 1.5$ ($\beta = 0.67$). We show the time evolution of (i) the mass accreted onto the BH ($M_{\rm acc}$); (ii) the mass accretion rate ($\dot{M}_{\rm BH}$) in units of a fiducial Eddington rate, $\dot{M}_{\rm Edd} = L_{\rm Edd}/0.1c^2$, where $L_{\rm Edd} \equiv 4\pi GMm_pc/\sigma_T$ is the standard Eddington luminosity, G is Newton's gravitational constant, m_p is the proton mass, c is the speed of light, and σ_T is the Thomson cross section, and the constant 0.1 represents a canonical radiative efficiency for nonspinning BHs; (iii) the fraction of mass removed from the star ($f_{\rm rm}$); (iv) the orbital separation (r); (v) the evolution of the SMA normalized to its initial value (a/a_0); and (vi) the evolution of the eccentricity (e). The bottom four panels of Figure 7 reflect the properties of the stellar remnant and are therefore only computed before total disruption; times after total disruption of the star are labeled with hatched lines. Finally, we show the times of pericenter and apocenter passages with red dashed lines and blue solid lines, respectively.

In the first model, $\mathcal{M}(1, 0.4, 1)$, the mass of the BH grows monotonically with time, while the accretion rate increases

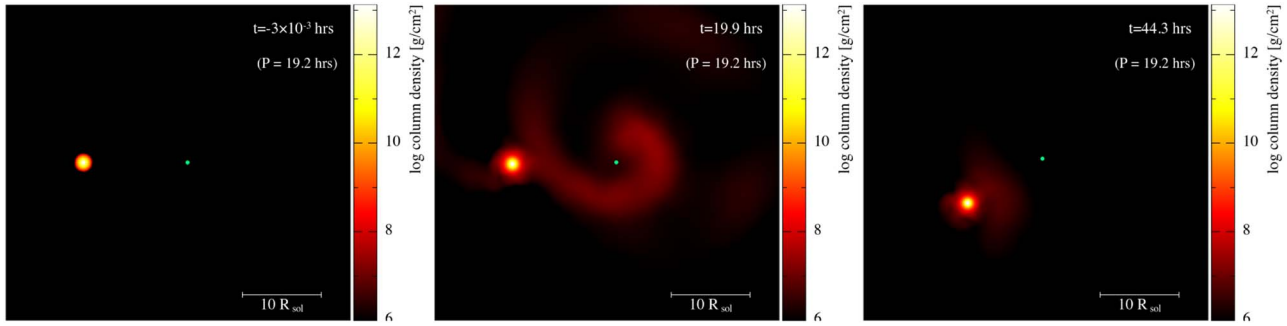

Figure 5. $\mathcal{M}(1, 0.6, 0.67)$: tidal peeling of the same BH–star binary described in Figure 3, but with initial eccentricity $e_0 = 0.6$ and $\beta = 0.67$. The initial orbital period (in parentheses) is 19.2 hr.

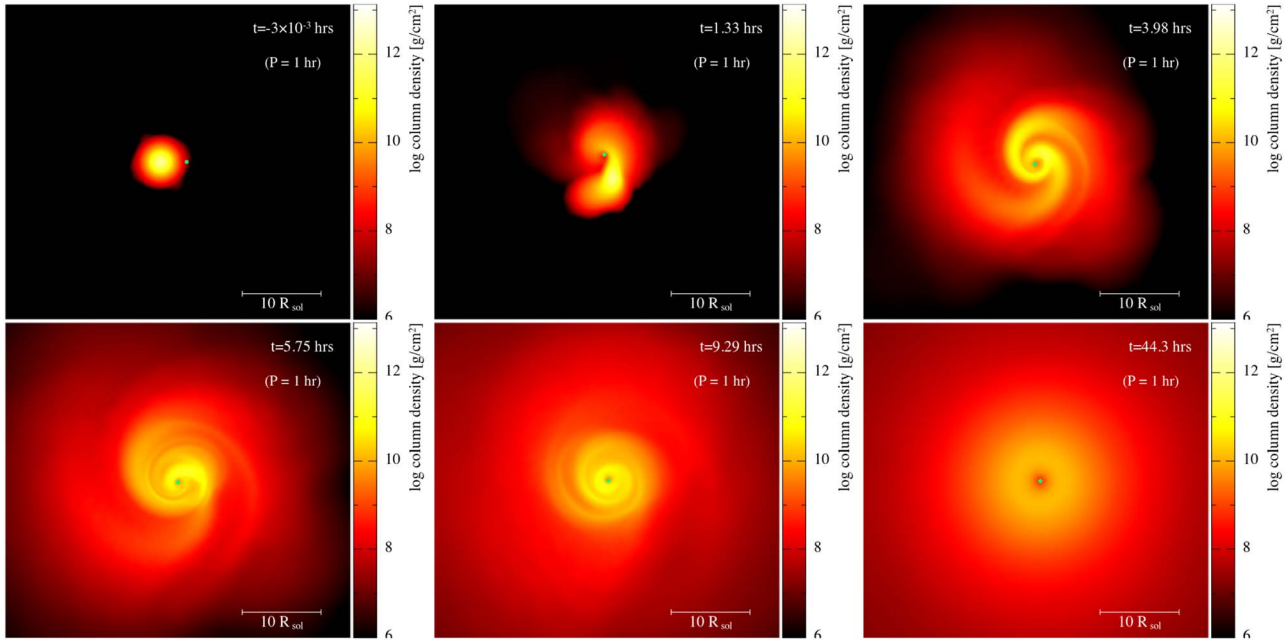

Figure 6. $\mathcal{M}(5, 0, 1)$: tidal peeling of a BH–star binary with a higher stellar mass, $M_s = 5\ M_\odot$, initially circular orbit ($e_0 = 0$), and a pericenter distance equal to the tidal radius $\beta = 1$. The initial orbital period of the binary is $\sim$1 hr. The star is completely disrupted soon after the beginning of the simulation.

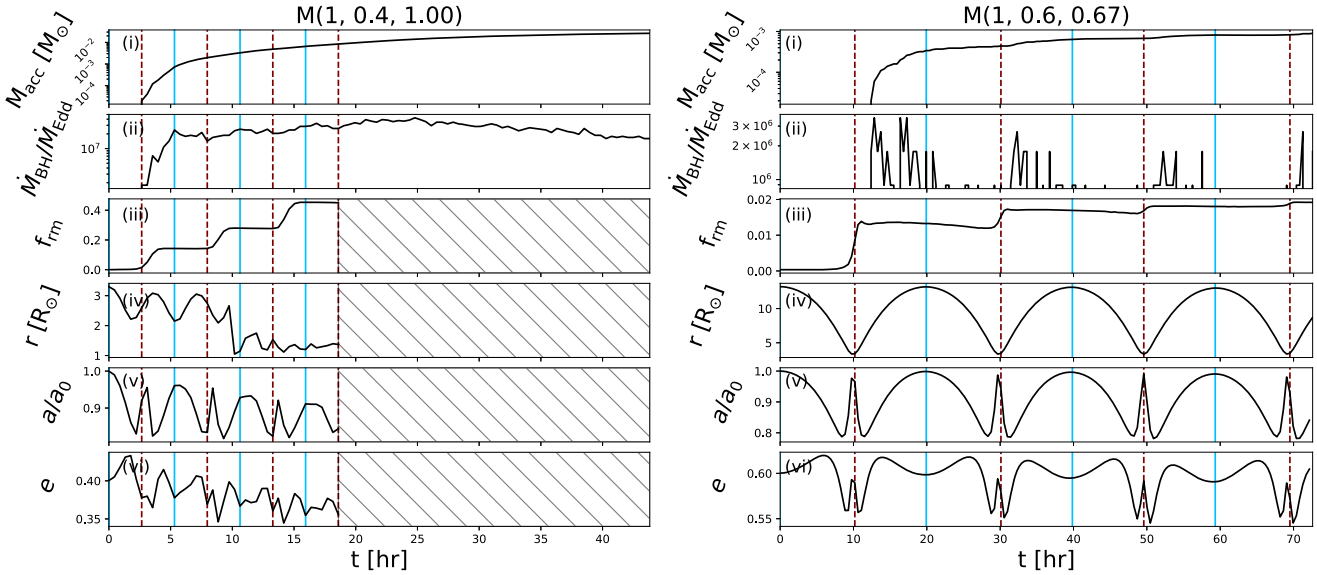

Figure 7. Time evolution of key physical quantities characterizing TPEs, for models $\mathcal{M}(1, 0.4, 1)$ (left) and $\mathcal{M}(1, 0.6, 0.67)$ (right). The six panels, from top to bottom, show the (i) mass accreted by the BH, (ii) accretion rate in Eddington units, (iii) the fraction of mass removed from the star, (iv) the separation between the remnant and the BH, (v) the evolution of the SMA, and (vi) the eccentricity. The pericenter and apocenter passages are labeled with red dashed and blue solid lines, respectively. The hatched regions represent total disruption of the star.

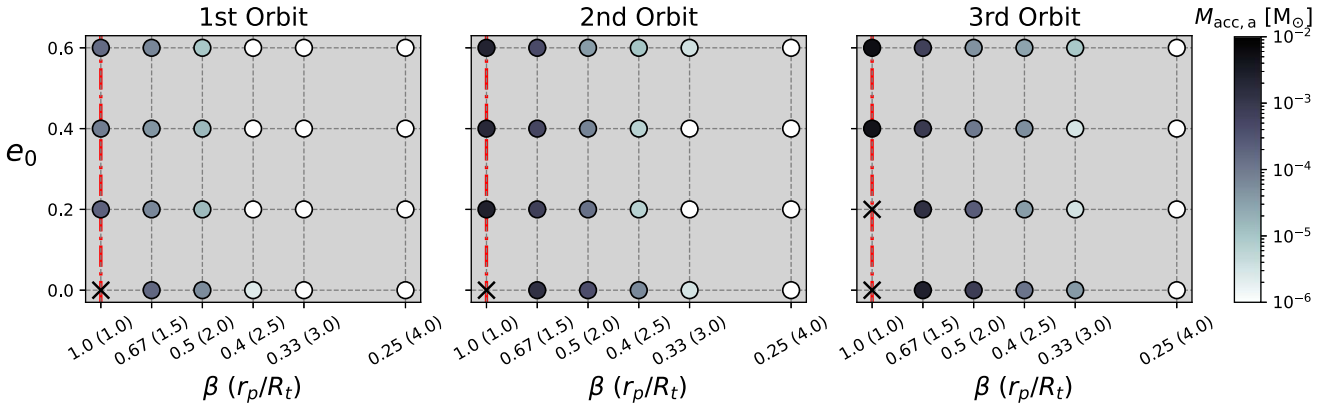

Figure 8. The change of mass accretion onto the BH per orbit, $M_{acc,a}$, for TPEs with a 1 $M_\odot$ star, as a function of initial e_0 and β, evaluated for the first three orbits of the stellar remnant around the BH. We show the pericenter distances corresponding to each β in the parentheses. The darker end of the color bar represents larger $M_{acc,a}$ values, which decrease as the initial orbit becomes wider and more eccentric. In the most compact configurations, the star is totally disrupted (crosses), while in the least compact orbits, zero mass is accreted by the BH (open circles). The onset of mass transfer is analytically expected to occur when $r_p \approx R_t$ (red dashed–dotted line).

until reaching a plateau around 5 hr ($\sim P$), where it exceeds the Eddington limit by more than seven orders of magnitude. In fact, the values of $\dot{M}_{BH}$ that we find are typically super-Eddington within the first few orbits of disruption if r_p is within $\sim 3\ R_t$. In this model, the stellar remnant orbits around the BH on a $\sim$5 hr orbital timescale, during which the binary separation shrinks and the fraction of stellar mass removed becomes larger until the star gets totally disrupted after approximately four orbital times. The large fluctuations in a and e indicate that the star–BH orbit is not Keplerian due to tidal effects and shocks, resulting in the dissipation of orbital energy and asymmetric mass loss.

For an initially less compact binary, e.g., $\mathcal{M}(1, 0.6, 0.67)$ (right-hand side of Figure 7), the stellar remnant does not undergo total disruption in the first few orbits. In fact, the mass accretion rate spikes after each pericenter passage (minima in r) with a small time delay, while the peak level decreases over time. A similar occurrence of delay has been reported in simulations of binary stars, where the peak of the mass transfer rate is found shortly after each binary orbit's pericenter (Lajoie & Sills 2011). The repeated flares are due to periodic mass loss on an eccentric orbit. We find that the periodicity weakens for smaller e_0 given the same β. The fluctuations in a and e indicate non-Keplerian orbital evolution, even for a slightly tidally disrupted star's orbit.

6.2. Dependence on the Initial Conditions

In this section, we investigate the dependence of the six key quantities mentioned above on different initial conditions, namely M_s, e_0, and β, providing characteristics of the EM emission of TPEs. We measure these quantities during the first three orbits of the remnant around the BH, from one apocenter to the next (between the blue solid lines in Figure 7). In particular, we compute the change per orbit of mass accreted onto the BH, the BH accretion rate, and the fractional stellar mass removed, which are denoted $M_{acc,a}$, $\dot{M}_{BH,a}$, and $f_{rm,a}$, respectively. This allows us to take into account any enhancements in $\dot{M}_{BH}$ during each orbit, including the peaks near the pericenters as seen on the right-hand side of Figure 7. We also evaluate the total change in SMA ($\Delta a/a_0$) and eccentricity (Δe) during each orbit.

We again draw the comparison between TPEs with two tidal disruption events: (i) a parabolic TDE (e.g., Bartos et al. 2017; Mainetti et al. 2017; Yang et al. 2020; Kremer et al. 2022), where more than half of the star's mass can be lost at the first pericenter passage, and (ii) our simulations of circular microTDEs ($e_0 = 0$ and $\beta = 1$) where the star is completely disrupted within the first three orbits. In comparison with these events, in a TPE, the star typically loses mass to the BH more gradually over many orbits around the BH. The degree of mass loss from the star and the mass accretion onto the BH can be different, depending on the choices of M_s, e_0, and β.

Figure 8 shows the orbital change of the mass accretion, $M_{acc,a}$, of the TPEs for the 1 $M_\odot$ star and the 10 $M_\odot$ BH, under different assumptions for β (x-axis) and e_0 (y-axis). In the most compact models ($\beta = 1$), the star gets totally disrupted within the first three orbits, which are denoted with crosses. These are roughly consistent with the analytical expectation that the star undergoes tidal disruption when the pericenter distance of the orbit is comparable to the tidal radius, i.e., $r_p/R_t \sim 1$ (red dotted–dashed line). More generally, $M_{acc,a}$ is larger for initially more compact orbits, meaning smaller r_p (larger β) and smaller e_0. The latter are equivalent to having a smaller initial orbital separation, since we initially place the star at the apocenter distance $r_{apo} = a_0(1 + e_0)$. However, we see a smaller dependence of $M_{acc,a}$ on the initial eccentricity than on the initial pericenter distance. The amount of mass accreted by the BH inevitably increases over time once mass transfer begins, resulting in the highest values of $M_{acc,a}$ in the third orbit. In the models with the largest pericenter distances, $r_p/R_t \gtrsim 3$, there is no mass accretion onto the BH in the first three orbits, as denoted by the open circles.

We see similar trends in the fraction of stellar material removed from the star ($f_{rm,a}$; Figure 9). Tidal peeling can remove stellar mass slowly over a few orbital times, which can be seen from the persistent increase of $f_{rm,a}$ over the first three orbits. Generally, a larger fraction of the star is removed when the initial orbit has smaller r_p and e_0, and as time progresses. Note that even in the widest binaries ($r_p/R_t \gtrsim 3$), a small amount of stellar mass is removed under tidal effects, which is beyond the analytical prediction (e.g., Zalamea et al. 2010) for the onset of mass loss (red dotted–dashed line), although the mass accretion onto the BH can be zero (as seen in Figure 8). Finally, we again observe larger variations in $f_{rm,a}$ due to r_p than due to e_0.

Figure 10 shows that typically $\dot{M}_{BH,a}$ ranges from $\sim 10^4$ to 10^8 times the Eddington accretion rate of the BH. The values of

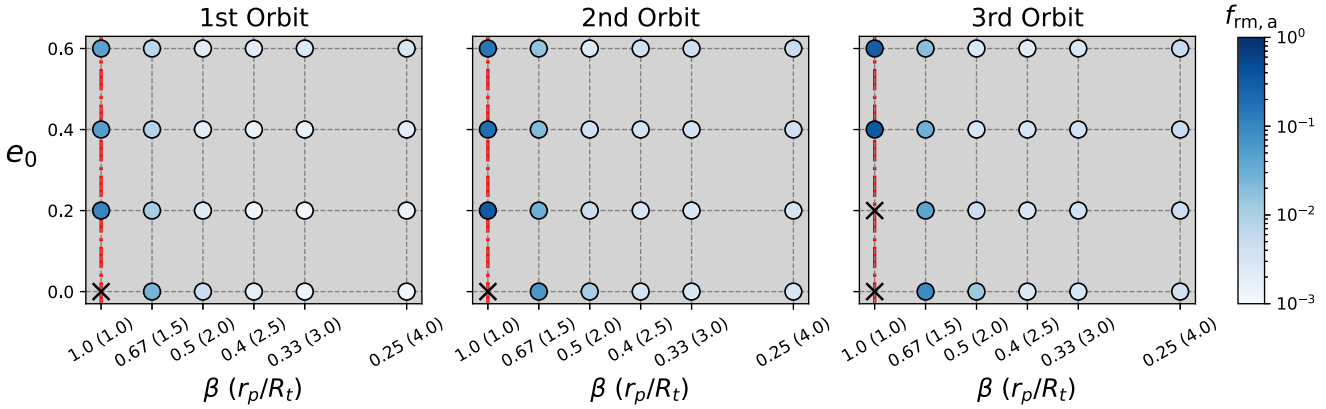

Figure 9. Similar to Figure 8, but we show the orbit-averaged fraction of mass removed from the star and the BH, $f_{\rm rm,a} = M_{\rm rm}/M_s$, where $M_{\rm rm} = M_s - M_{\rm rem,s} + M_{\rm acc,BH}$, where M_s is the total mass of the star, $M_{\rm rem,s}$ is the remnant mass, and $M_{\rm acc,BH}$ the mass accreted onto the BH. The crosses represent total disruption. The red dotted–dashed lines again represent the onset of the mass transfer limit at $r_p \approx R_t$.

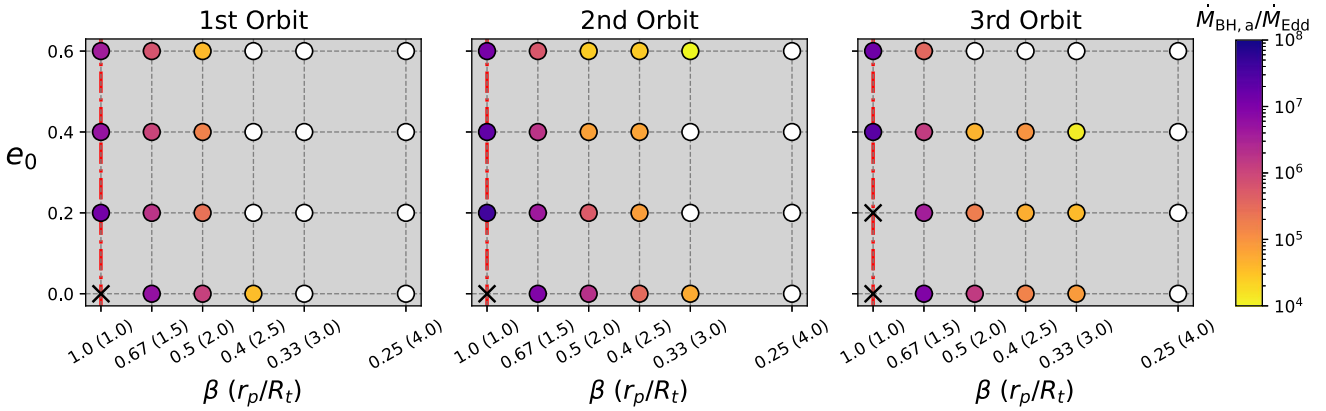

Figure 10. Mass accretion rate onto the BH, $\dot{M}_{\rm BH}$, as a function of initial eccentricity and penetration factor (the corresponding pericenter distances are quoted in parentheses), taken at the first to third pericenter passages. $\dot{M}_{\rm BH}$ is given in units of $\dot{M}_{\rm Edd} \sim 2.2 \times 10^{-7} M_\odot$ yr^{-1} for a 10 $M_\odot$ BH. The open circles represent a mass accretion rate of zero. The crosses represent total disruption.

$\dot{M}_{\rm BH,a}$ are overall higher when the initial binary orbit is more compact and less eccentric, although, as seen in Figures 8 and 9, the impact of the initial value of r_p is larger than the impact of e_0. Like the trend in both the BH mass accretion and fraction of stellar mass loss, the values of $\dot{M}_{\rm BH,a}$ tend to increase over time, except in some models with $e_0 = 0.6$, e.g., $\mathcal{M}(1, 0.6, 0.67)$ in Figure 7, where the tidal influence is the weakest due to the large initial separation between the star and the BH.

Most TPE models in our simulations indicate partial disruption of the star, which suggests EM emission from TPEs persisting over many orbits. Although we only simulate the first few orbital times of the TPEs in this work, we investigate the orbital evolution of the stellar remnant during this time, and we attempt to find patterns in the evolutions of the SMA and the eccentricity that could predict whether the binary separation widens or becomes more compact. Future work should investigate the long-term behavior of star–BH TPEs, in order to determine (i) the full duration of their EM emission, and (ii) whether or not the star will be eventually totally disrupted by the BH.

In Figure 11, we demonstrate the variations in SMA (Δa) per orbit evaluated during the first three orbits of the 1 $M_\odot$ star around the BH in the TPEs. We investigate the change in Δa, normalized by the initial SMA a_0 of each model, due to different initial values of β and e_0. The color bars show percentage values of $\Delta a/a_0$, which typically fluctuate within $\sim$4%. We observe that in most models, Δa remains roughly zero (yellow points), corresponding to very small variations in a during one orbit, meaning that the orbital separation at one apocenter is not too different from the next one. The redder points in Figure 11 correspond to the models where the orbits are widening ($\Delta a > 0$) while the bluer points correspond to shrinking orbits ($\Delta a < 0$). There is a lack of overall trends that dictate whether Δa increases or decreases with the two initial conditions, except that the most compact orbits tend to decay.

Figure 12 shows the change of eccentricity Δe in the first three orbits for the same models in Figure 11. Most models show small variations in Δe (yellow points), except for the initially circular models (bottom points) and the most compact models with different e_0 (points in the first column), which are consistent with the behaviors seen for Δa. The stars in these models are the most tidally influenced by the BH, where Δe shows significant fluctuations in all three orbits, where some orbits become more eccentric then later circularize, and vice versa.

6.3. Sources of Luminosity

In a TPE, super-Eddington accretion onto the BH powers an outflow from the accretion disk. The EM emission from the TPE is delayed by the photon diffusion time ($\tau_{\rm diff}$), which

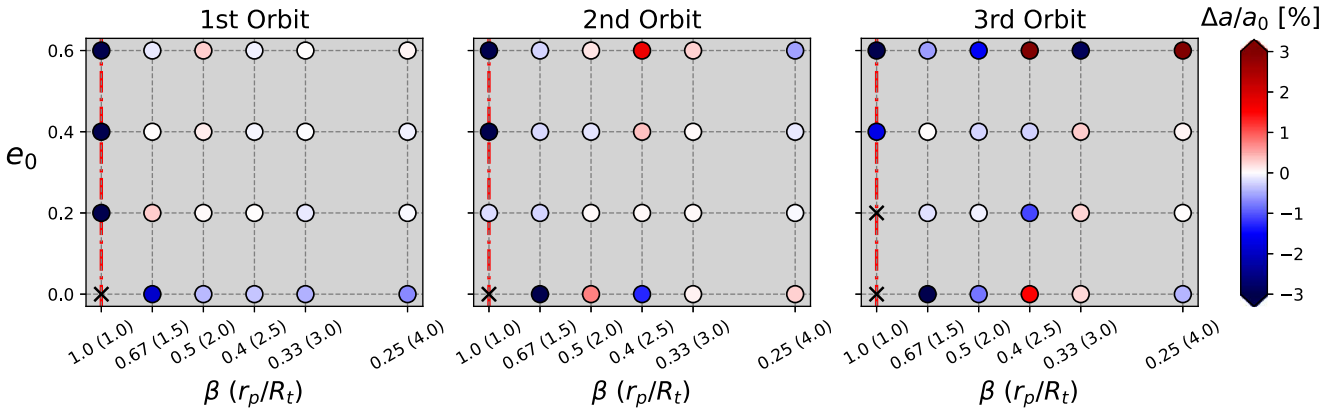

Figure 11. The change of SMA (Δa) normalized by its initial value (a_0) during the first, second, and third orbit around the BH, given as a percentage. The white points represent (near) zero changes in the SMA during the orbit, while the redder (bluer) points represent an expanding (shrinking) orbit.

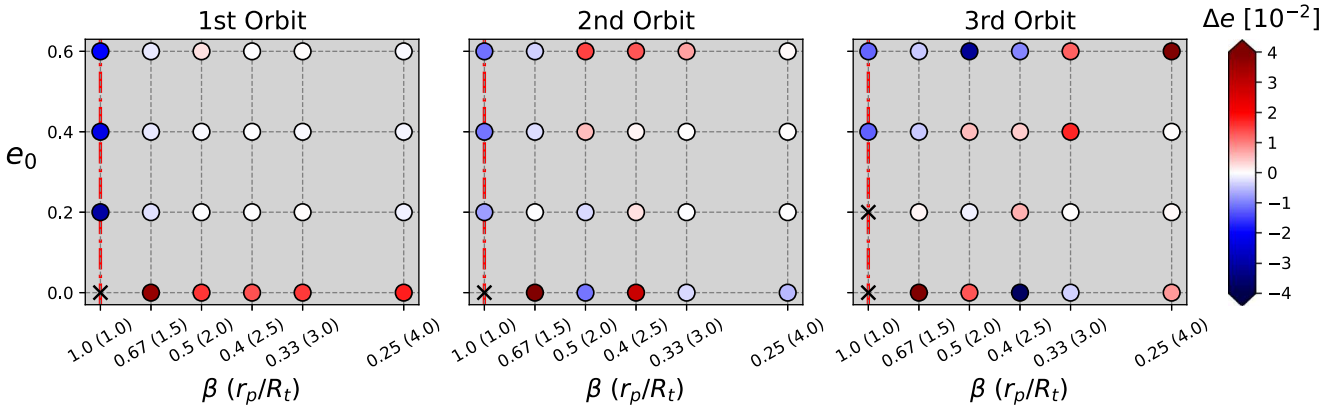

Figure 12. The change of eccentricity (Δe) during the first, second, and third orbit around the BH. The white colors represent (near) zero changes in the eccentricity during the orbit, while the redder (bluer) points represent the orbit becoming more (less) eccentric.

dilutes the emission from the accretion disk. From our simulation, $\tau_{\rm diff} = \tau H/c \sim 10^5$ yr, similar to the photon diffusion time in the Sun. In this relation, $H \sim 1.5\ R_\odot$ is the thickness of the accretion disk formed from the TPE. τ is the optical depth to electron scattering, computed assuming fully ionized gas as

$$\tau = \int_r^\infty \rho(r') \frac{\sigma_T}{m_p} dr' \approx 10^{11}, \quad (1)$$

where σ_T is the electron scattering cross section. ρ is the three-dimensional density of the accretion disk taken directly from our simulations, which is typically very high since a large fraction of the star is stripped to form the disk in a TPE. Overall, the photon diffusion time $\tau_{\rm diff}$ is much longer compared to the viscous timescale of the accretion disk (e.g., Equation (4) in Shakura & Sunyaev 1973; D'Orazio et al. 2013)

$$\tau_{\rm visc} \simeq 1060 \left(\frac{\mathcal{M}}{10}\right)^2 \left(\frac{0.01}{\alpha}\right) t_{\rm orb} \lesssim O(100) \text{ days}, \quad (2)$$

although the value of the viscous timescale depends on the local properties of the accretion disk. In Equation (2) $\mathcal{M}$ is the Mach number, α is the Shakura–Sunyaev viscosity parameter, and $t_{\rm orb}$ is the orbital time, which is typically a few hours. While we use Equation (2) for the convenience of expressing $\tau_{\rm visc}$ with the orbital time, this relationship is equivalent to $\tau_{\rm visc} = (2/3) r^2/\nu$, where $\nu = (\alpha \cdot c_s^2)/\omega$, and we measure the sound speed and orbital frequency (and in turn also the Mach number) from our simulations. However, given the super-Eddington accretion rate of a TPE, a relativistic jet may be launched and break out from the disk, possibly allowing the TPE to shine through. Since $\dot{M}_{\rm BH} \gg \dot{M}_{\rm Edd}$, there could be a strong accretion disk outflow that might also modify the EM emission of a TPE. If the TPE is embedded in an AGN disk, the star and the BH will accrete mass from the disk. We use Equation (24) in Tagawa et al. (2020) to estimate that the mass accretion rates onto the star and the BH are both approximately $10^3 \dot{M}_{\rm Edd}$, with the BH's accretion rate $\sim$5% of the star's. We assume that the TPE is located $r \sim 10^{-2}$ pc from a central massive BH of mass $10^6\ M_\odot$, where the disk density is $\rho_{\rm AGN} \sim 10^{12}\ M_\odot$ pc^{-3} and the aspect ratio is $\simeq 10^{-3}$. The accretion rates from the AGN disk are also super-Eddington, although they are still few orders of magnitude lower than the $\dot{M}_{\rm BH}$ in the TPE. Modeling these aspects of TPEs would require higher resolution, radiative transfer, and/or perhaps a different numerical code that can include the low-density background AGN disk, which could be addressed in future work.

7. Massive Stars

Due to different stellar radii and density profiles in massive stars, we investigate the behavior of TPEs where stars more

massive than a solar mass are involved, i.e., $M_s = 5$, 10, and 15 $M_\odot$. Figure 13 shows (i) the properties of TPEs depending on the initial stellar mass and initial pericenter distance, at fixed $e_0 = 0.4$ (left panels), and (ii) the same properties depending on the initial M_s and e_0, at fixed r_p (right panels). From top to bottom, we show the change in the mass accretion onto the BH, the fraction of mass removed from the star, and the mass accretion rate per orbit. The crosses indicate that more massive stars are more likely to undergo total disruption given the same initial orbital configurations, due to the fact that a more massive star's surface is closer to the BH, even though its density profile is steeper, as shown in Figure 14. This figure shows the density profiles of the initial stars, which have masses $M_s = 1$, 5, 10, and 15 $M_\odot$, as labeled.

In Figure 13, we normalize the BH mass accretion by the initial mass of the star, $M_{\rm acc,a}/M_{\rm s}$, in the top two panels. Therefore, any change in $M_{\rm acc,a}/M_{\rm s}$, as well as in $f_{\rm rm,a}$ and $\dot{M}_{\rm BH}$, with the initial M_s (along the y-axes) reflects different interior structures of the stars due to different masses. There are minimal changes in $M_{\rm acc,a}/M_{\rm s}$, $f_{\rm rm,a}$, and $\dot{M}_{\rm BH}$ along the M_s axis at any fixed r_p or e_0, especially for $M_s \geqslant 5$ $M_\odot$. This indicates that the stellar interiors, mainly the envelopes that are being tidally stripped, are not significantly different for stars more massive than 5 $M_\odot$, although we cannot gauge this difference if the stellar cores are destroyed, i.e., in the cases with total disruption.

Overall, these three quantities show more variation due to different initial r_p and e_0 compared to the effect of stellar mass. At fixed e_0, $M_{\rm acc,a}/M_{\rm s}$, $f_{\rm rm,a}$, and $\dot{M}_{\rm BH}$ decrease as the initial pericenter distance becomes wider, where $M_{\rm acc,a}/M_{\rm s}$ and $\dot{M}_{\rm BH}$ reduce to zero (open circles) even for more massive stars. Similarly, at fixed r_p, these quantities decrease as e_0 gets larger, due to the fact that elliptical orbits with larger eccentricities (given the same pericenter distances) are longer orbits. Consistent with the $M_s = 1$ $M_\odot$ cases, the impact of r_p is overall more significant than the impact of e_0. Generally, having a more massive star in the TPE results in more mass accretion onto the BH and higher accretion rates. Our figures show the fractions of star lost or accreted by the BH, which indicate the importance of the different stars' interior structures.

Finally, as a broad comparison we evaluate the mass-loss rate of a 1 $M_\odot$ star using the analytical solution described in Zalamea et al. (2010), and compare this solution to our simulation results. This analytical solution predicts the rate of mass loss of a WD when it is tidally disrupted by a SMBH, which can also be approximately applied to our TPE scenario. Zalamea et al. (2010) predict that an outer shell of the star with thickness ΔR is removed at each tidal stripping, as long as $R_s < 2\ R_t$, where $\Delta R = R_s - R_t \ll R_s$. The main differences are that (i) our stellar density profile describes a solar-like MS star that is governed by gas + radiation pressure, instead of a WD governed by electron degeneracy pressure, (ii) our mass ratio is much closer to unity, and (iii) the pericenter is much closer to the tidal radius, since we have a stellar-mass BH rather than an SMBH. Adopting these changes, the analytical calculation of the stellar mass-loss rate ($\dot{M}_{\rm loss}$; red) from our simulation is shown Figure 15, along with the mass-loss rate we evaluate from the simulation output (black). This figure shows reasonable consistency between the two, where the analytical solution is roughly half the simulation result at first. However, the analytical solution shows a slower drop in amplitude.

8. Discussion

8.1. Comparing TPEs to MicroTDEs and TDEs by IMBHs and SMBHs

The orbit of the star in a microTDE is typically expected to be parabolic when tidally disrupted by the BH. From a recent study of hydrodynamics simulations of microTDEs (e.g., Kremer et al. 2022), they are likely ultraluminous transients, similar to our finding for TPEs. We find that similar to microTDEs, TPEs have super-Eddington accretion rates, up to $\sim 10^8 \dot{M}_{\rm Edd}$, which is order-of-magnitude comparable to that of "normal" microTDEs; see Figure 11 in Kremer et al. (2022). However, the method that Kremer et al. (2022) use to measure the accretion rate by assuming that some disk mass is accreted by the BH within the viscous time, or Equation (3), is different from our method of using a sink particle to measure BH accretion rate. They assume

$$\dot{M}_{\rm BH} \propto \left(\frac{M_{\rm disk}}{t_{\rm visc}}\right)\left(\frac{R_{\rm in}}{R_{\rm disk}}\right)^s. \quad (3)$$

In this relation, we choose an accretion disk with radius $R_{\rm disk} = R_t = 2.2\ R_\odot$ that includes particles within the initial Roche lobe radius around the BH; see the last panel of Figure 3. $M_{\rm disk}$ is the disk mass, which eventually reaches 0.8 M_s. $t_{\rm visc}$ is the viscous timescale that we calculate using Equation (2), where the Mach number $\mathcal{M} = v_{\rm orb}/c_s = 3$ is directly measured from our simulation and $\alpha = 0.1$. $R_{\rm in}$ is the inner edge of the disk: we choose $R_{\rm in} = 10\ r_{\rm sch}$, where $r_{\rm sch} = 2GM_{\rm BH}/c^2$. Finally, the choice of the power-law index s accounts for different levels of mass loss due to outflows. In Figure 16, we compare the accretion rates computed with Equation (3) to that found with the sink particle, for the TPE model $\mathcal{M}(1, 0.4, 1)$. The top panel shows the mass accretion rate onto the sink particle ($\dot{M}_{\rm BH,sink}$), and the bottom panel shows the accretion rate from the disk calculation ($\dot{M}_{\rm BH,disk}$) assuming three choices for the power-law index $s = 0$, 0.5, and 1. $\dot{M}_{\rm BH,disk}$ is overall comparable to $\dot{M}_{\rm sink}$, although it rises earlier as some mass falls within $R_{\rm disk}$ instantaneously after the simulation begins. We perform the same comparison for a parabolic microTDE model that was reported in Kremer et al. (2022), with $M_{\rm BH} = 10\ M_\odot$, $M_{\rm s} = 1\ M_\odot$, $e_0 = 1$, and $\beta = 1$; see Figure 17. We adopt a disk with radius $R_{\rm disk} \sim 3.7\ R_\odot$, the value used by Kremer et al. (2022), and $t_{\rm visc}$ evaluated with Mach number $\mathcal{M} = 1$. The two methods again yield similar accretion rates.

Despite having similar accretion rates, the orbital periods are generally shorter for a TPE, which are between a few to a few tens of hours, compared to periods of days to weeks for a microTDE. Some of the microTDE models in Kremer et al. (2022), such as the model with a more massive $M_s = 5\ M_\odot$ star and a 10 $M_\odot$ BH, show multiple passages and therefore periodic accretion onto the BH, just like in a TPE. However, the orbital period in this model is $\sim$4 days, significantly longer than TPE periods, so we will be able to distinguish them from a TPE. But generally, stars in most microTDEs undergo tidal stripping only once, leaving very different morphological evolution, accretion, and orbital signatures compared to a TPE.

Another important comparison should be made between TPEs and tidal disruptions of a solar-like star by an IMBH. Recent work by Kıroğlu et al. (2022) find, using

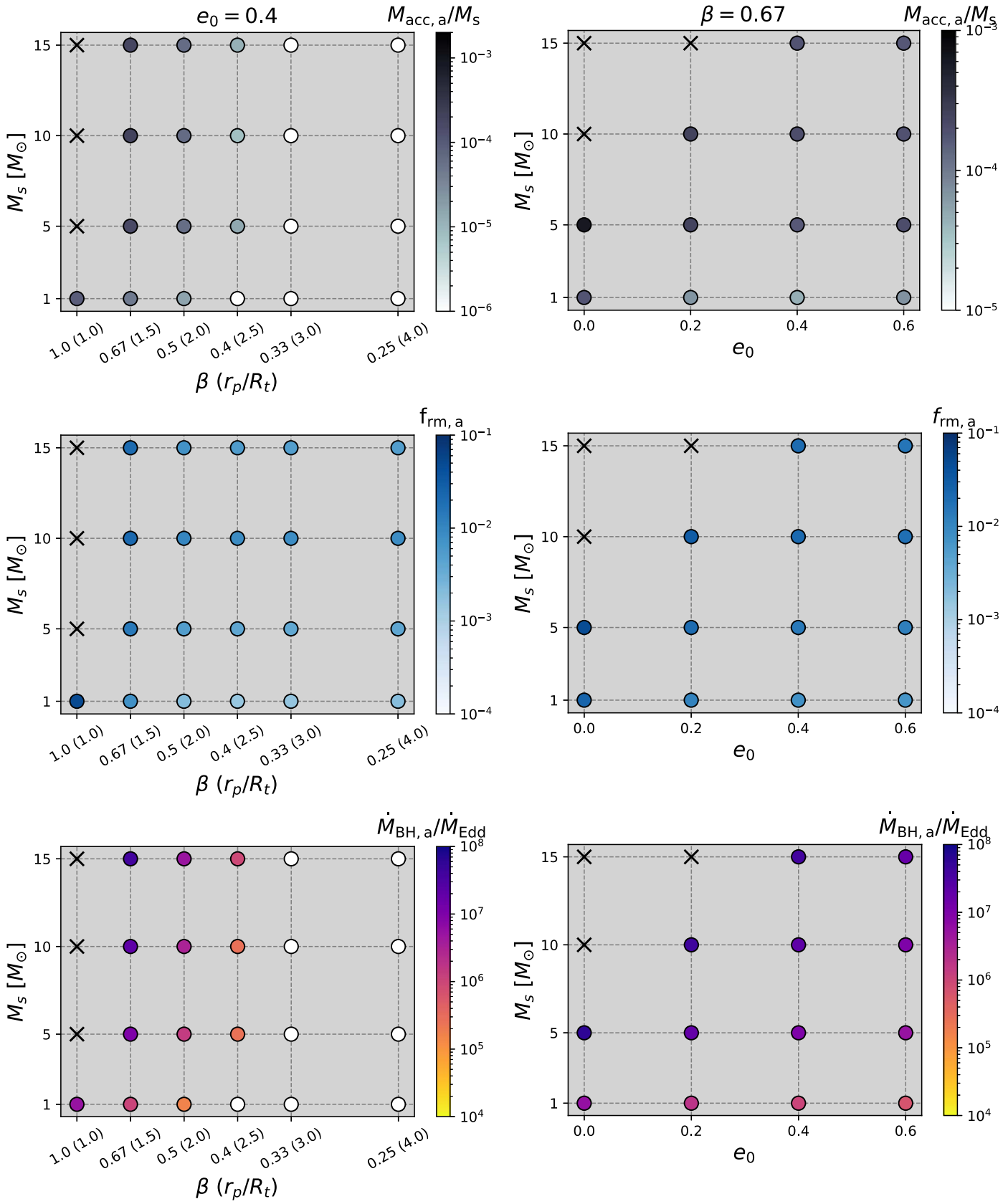

Figure 13. Mass accreted by the BH ($M_{\rm acc,a}$) normalized to stellar mass, the fraction of mass removed ($f_{\rm rm,a}$), and accretion rate onto the BH ($\dot{M}_{\rm BH,a}$) as a function of (1) the stellar mass and penetration factor at fixed initial $e_0 = 0.4$ (left column), and (2) the stellar mass and eccentricity at fixed pericenter $\beta = 0.67$. These are evaluated in the first orbit of the simulation. As in previous figures, a cross indicates full disruption. In general, $M_{\rm acc,a}$, $f_{\rm rm,a}$, and $\dot{M}_{\rm BH,a}$ decrease for larger initial separations and eccentricities. The more massive stars are the more likely to be completely disrupted due to their larger stellar radius compared to the tidal radius. There is a lack of trends in $M_{\rm acc,a}$, $f_{\rm rm,a}$, and $\dot{M}_{\rm BH,a}$ depending on M_s for $M_s > 1\ M_\odot$, indicating that the stellar structures are not significantly different for those stars.

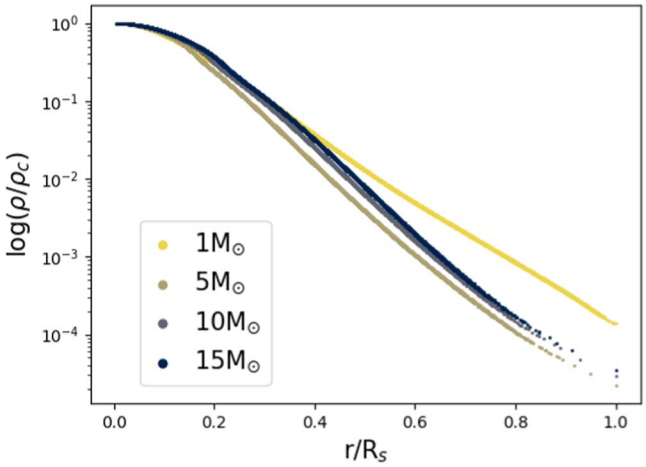

Figure 14. Initial density profiles of the stars used in the TPE simulations, which have $M_s = 1$, 5, 10, and 15 $M_\odot$ as labeled in the legend. The log-scale density is normalized by the core density of the star, which is a function of radius normalized by the stellar radius.

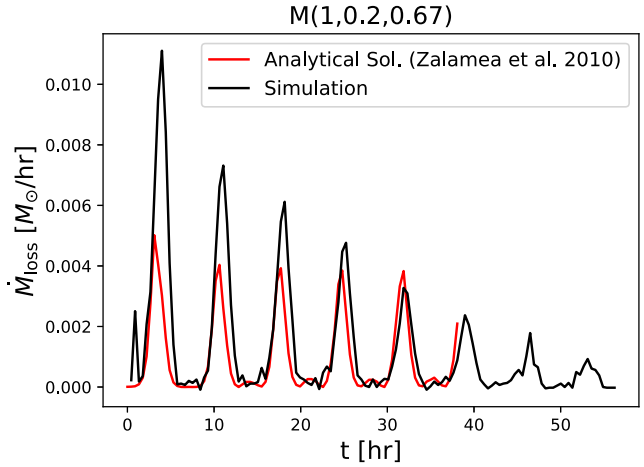

Figure 15. Comparing the rate of stellar mass loss from our simulation, $\mathcal{M}(1, 0.2, 0.67)$ (black), to that predicted by the analytical solution (red) in Zalamea et al. (2010).

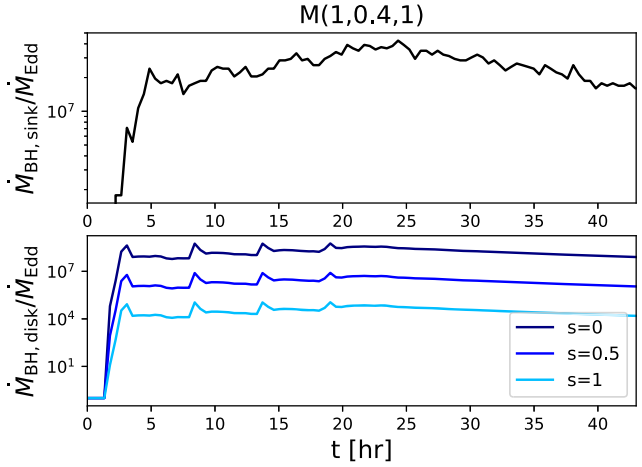

Figure 16. Accretion rates of the BH in TPE model $\mathcal{M}(1, 0.4, 1)$ evaluated using (i) the mass accreted onto the sink particle (top panel) and (ii) the mass accretion calculated with Equation (3), following Kremer et al. (2022; bottom panel). The bottom panel adopts three choices of the power-law index: $s = 0$, 0.5, and 1.

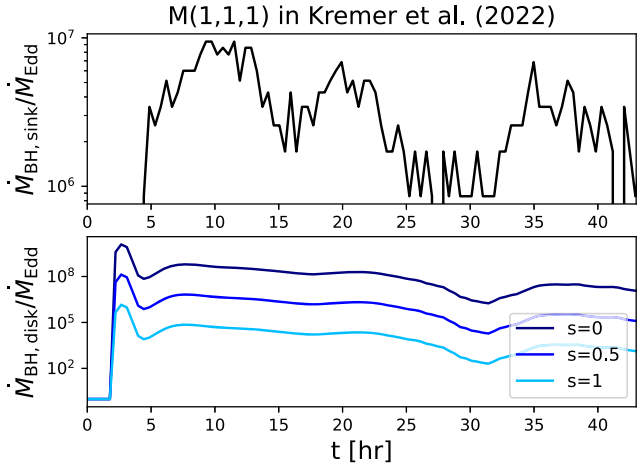

Figure 17. Same comparison as Figure 16, but for the parabolic microTDE model $\mathcal{M}(1, 1, 1)$ from Kremer et al. (2022). Similar to Figure 16, the accretion rates from the sink and disk methods show roughly consistent results.

hydrodynamics simulations, that in all cases where a 1 $M_\odot$ star is disrupted by an IMBH, the stellar remnant is eventually ejected to be unbound, either after the first pericenter or after many pericenter passages. In our TPE simulations, all stars remain in a binary with the BH, or are eventually completely disrupted by the BH. If the star survives for many pericenter passages with the IMBH, then the star is only partially disrupted and the accretion rate increases with the number of orbits. This is also not the case in TPEs (see the right-hand side of Figure 7), where $\dot{M}_{\rm BH}$ decreases with the number of orbits. Finally, the orbital periods of tidal disruptions by IMBH typically span a wide range, from tens of hours to 10,000 yr. The shortest-period events with comparable periods to TPEs correspond to the lowest BH mass ($M_{\rm BH} \lesssim 10\ M_\odot$) and smallest pericenter distance ($r_p/R_t \ll 1$). Therefore, these events are basically the microTDEs in Kremer et al. (2022) and their similarities and differences to TPEs are already mentioned above.

The best indicator that a microTDE is present in an AGN, rather than a TDE of a solar-like star by an SMBH, is if the mass of the SMBH is above the Hill's limit $\gtrsim 10^8\ M_\odot$, beyond which the Schwarzschild radius of the BH is greater than the tidal radius. However, microTDEs or TPEs have distinguishable signatures even if they exist near a smaller SMBH. First, the spectra of microTDEs and TDEs are expected to be very different, because the remnants produced in microTDEs tend to be optically thick—this is even more so the case in TPEs, which lead to a hotter accretion disk that cools less efficiently (Wang et al. 2021) and result in emission in the more energetic range of X-rays. Additionally, like in most microTDEs, the SMBH in a TDE typically will disrupt the star once and strip of order half to all of its mass, while partial disruptions are more common in TPEs. Partial disruptions in TDEs, however, will have periodic flares on a yearly scale, such as the recent observation of repeated bursts in AT2018fyk (Wevers et al. 2022), much longer than the expected periods of microTDEs and TPEs.

Overall, our simulations show that TPEs are novel transient phenomena that can be distinguished from other ultraluminous transients such as microTDEs, tidal disruptions by IMBHs and SMBHs, and partial disruptions in TDEs.

8.2. Simulation Caveats

Theoretical investigations of TPEs have many important implications, such as understanding interactions in compact star–BH binaries in star clusters or AGN disks and observations of ultraluminous transient events especially those near the Galactic center. While our results offer first-hand understanding of TPEs with simulations, they should be treated as numerical experiments rather than accurate physical descriptions of TPEs in a cluster or embedded in an AGN disk. We list the following caveats of our simulations that should be improved in the future.

First, we start the simulations with already very compact orbits, while in reality, they should be expected to occur only at the end of some dynamical process such as a long AGN disk-mediated inspiral or interactions between multiple stars or compact objects in a star cluster. Since the BH and star should approach each other from a much larger distance, we might expect the star to have already been partially disrupted by the BH, although no mass will be accreted by the BH beyond the separation of $r_p \sim 3\ R_t$, as shown by our results. Due to computational limitations, we are not able to evolve the binary from very small β-values. However, we ran one of the 96 models, the lowest-β model (M=1, $e_0 = 0$, and $\beta = 0.25$) for $\sim$30 orbits, since the initial β is sufficiently small and the mass loss over the first three orbits is nearly zero. Although computational limitations do not allow us to see whether or not the next higher-β configurations can be achieved, we see that the star does not remain intact and it would likely have already been significantly deformed or disrupted before getting to more compact separations. This further motivates our goal to perform a grid of long-baseline simulations, but the process of inspiraling from a larger distance requires a significant additional computational investment and is postponed to future work.

The binary could, however, accrete from the external AGN gas, if embedded in an AGN disk. In future work, we will investigate the effect of torques from the circum-binary gas on the binary, which can shrink the orbital separation. For example, one could include low-density AGN disk gas as a background of the TPE simulations, instead of using a vacuum. This is challenging with SPH simulations, but could instead be feasible with grid-based codes.

Finally, it would also be important to model radiation outflows from the optically thick accretion disk and shock formation due to the relative motion of the star or BH and the debris, in order to describe TPEs more accurately. In particular, in most of our runs, the accretion rate exceeds the Eddington rate by several orders of magnitude. In an idealized spherical flow, this would not result in super-Eddington luminosity since most of the radiation would be trapped and advected inward with the flow (Begelman 1979). Our spatial resolution is far larger than the Schwarzschild radius, but given that the accreted gas has significant angular momentum, one can speculate that a compact disk would form, with most of the radiation produced inside the so-called trapping radius ($\sim(\dot{M}/\dot{M}_{\rm Edd})R_s$) still advected into the BH, but with radiation-driven winds, as well as radiation, with luminosity near or somewhat above $L_{\rm Edd}$, emerging. This is suggested by recent hydrodynamical simulations that cover accretion rates up to several 1000 $\dot{M}_{\rm Edd}$, e.g., Jiang et al. (2014), Kitaki et al. (2021), and Hu et al. (2022); see also Figure 5 in Inayoshi et al. (2020) for a summary. These emerging winds and radiation can directly impinge on the gas on larger scales and change the dynamics; the escaping winds also may carry sufficient momentum and angular momentum to change the orbital evolution of the star–BH system. Future work should perform simulations or make analytical predictions for TPEs considering all of these additional factors above.

8.3. Detectability of TPEs as Transients in AGNs

AGNs are extremely dynamical locations to host luminous transients. Identifying TPEs among different transient events in AGNs will require careful examination of their EM signatures. AGNs around heavy SMBHs ($M_{\rm SMBH} \gtrsim 10^8\ M_\odot$) are shown to be the ideal place for identifying microTDEs (Yang et al. 2022) and other transients. In order to observe TPEs, they need to outshine the AGN disk. Since our results show that TPEs result in super-Eddington accretion onto the BH, there could be superluminous jet launching from the BH. Therefore, the EM emissions from TPEs can be subjected to jet modulation, among many other mechanism such as accretion disk outflows and shocks, as mentioned in Section 6.3. Even though the accretion disk formed from the stellar remnant is optically thick, and the AGN can also trap the radiation, the emissions from TPEs can be more visible if (i) the jet can eject gas from the circum-binary disk (Tagawa et al. 2022) and (ii) stellar-mass BHs can open cavities in the AGN disk (Kimura et al. 2021)—both of these will reduce the opacity of the surrounding gas. Finally, if the AGN does not launch any jets, then TPEs can outshine the AGN more easily in the radio or in gamma rays.

Here, we focus on the observational signatures of two microTDE candidates observed in AGNs that might also indicate TPE origins. MicroTDE candidates in AGNs with an SMBH too massive for tidal disruption of a solar-type star (ASASSN-15lh and ZTF19aailpwl; Yang et al. 2022), have peak luminosity $L_{\rm peak} \approx 5 \times 10^{45}$ erg s^{-1} and $L_{\rm peak} \approx 10^{45}$ erg s^{-1}. Yang et al. (2022) hypothesize that the higher peak luminosity of ASASSN-15lh indicates a microTDE, unless it is the result of tidal disruption of a star more massive than 1 $M_\odot$. From our simulations, we see that TPEs with a more massive star also produce higher accretion rates. The observations of ZTF19aailpwl show a longer rise time than a typical TDE, indicating a more gradual tidal disruption than a TDE by an SMBH, e.g., produced by a microTDE with low eccentricity such as a TPE. Additionally, Nicholl et al. (2023) discovered AT 2022aedm, a fast luminous transient that could possibly be explained by an encounter between a star and a stellar-mass BH, but the rise time of this event ($\sim$9 days) is much longer than the typical timescale of TPEs according to our simulation results. Finally, the rate of microTDEs is expected to be low in AGNs, at roughly 2 Gpc^{-3} yr^{-1} (Yang et al. 2022), and even lower in star clusters or stellar triple systems with BHs, although these predictions have large uncertainties. Only the brightest events are expected to be eventually observed, since the emission of most weaker microTDEs and TPEs will be dimmed significantly by the surrounding AGN gas. The mechanism that the emission from an event like a TPE propagates through an AGN disk is analogous to the propagation of a gamma-ray burst (GRB) afterglow in a dense medium (Perna et al. 2021; Wang et al. 2022). Therefore, bright TPEs might have observational signatures similar to that of ultralong GRBs.

9. Summary

In this paper, we perform the first hydrodynamics simulations of TPEs with the SPH simulation code PHANTOM to

investigate their morphology, accretion signature, and orbital evolution. We explore a range of initial conditions, including stellar mass, initial eccentricity, and penetration factor, which make up 96 simulation models in total. We examine the impacts of these initial parameters on the behaviors of TPEs.

First, we observe a "tidal-peeling" feature in our simulations where a solar-like or massive star is slowly and periodically tidally disrupted by a stellar-mass BH and its mass is slowly removed over many orbits. Due to their low eccentricity, the orbital periods of TPEs are generally shorter ($P \sim$ a few to a few 10s of hours) compared to microTDEs and TDEs. In the most compact orbits, $r_p \approx R_t$, the star gets completely disrupted very quickly, after $\sim$1–4 orbits; otherwise, the star ends up being partially disrupted. Out of the three initial conditions, the penetration factor has the largest effect on the accretion and orbital signatures of interest, namely mass accreted onto the BH, accretion rate, the fraction of mass removed from the star, the orbital separation, SMA, and eccentricity. As the orbit becomes more compact, there is more mass accreted by the BH, a higher accretion rate, and a higher fraction of mass removed from the star. A lower eccentricity has a similar effect, since a lower e_0 means that the orbit is shorter (recall that the star is placed at the apocenter at the start of the simulations). A few models with higher eccentricities show a periodic fluctuation in $\dot{M}_{\rm BH}$ that peaks after each pericenter passage.

The orbital separation, SMA, and eccentricity demonstrate less obvious trends, especially when $\beta < 1$ (less compact systems). It is clear from the fluctuations in a and e that the orbit of the star in the TPE deviates from Keplerian due to tidal influence and possibly also shocks as the stellar remnant encounters tidal streams. In the most compact configurations, $\beta = 1$, the orbital separation always shrinks regardless of the choice of e_0 and M_s, so both the SMA and eccentricity decrease with the number of orbits. In these cases, the star is always completely disrupted at the end, consistent with the analytical limit of onset mass loss of tidal stripping at $\beta = 1$ (e.g., Zalamea et al. 2010). Finally, if there is a more massive star in the TPE, the stellar radius is larger and, at fixed β, it is closer to the tidal radius. Therefore, the disruption is more rapid and total disruption of the star is more common. There is higher mass loss from the star as well as more accretion by the BH. However, for stars more massive than 1 $M_\odot$, the fraction of the initial stellar mass lost or accreted by the BH does not vary significantly due to different stellar masses. This indicates the similarity in the stellar structures of the more massive stars.

The resulting accretion rates of TPEs are typically highly super-Eddington, $\dot{M}_{\rm BH} \sim 10^{4-8}\dot{M}_{\rm Edd}$. However, since the accretion disk formed from the dense stellar material around of the BH is extremely opaque, the emission from TPEs will be affected by photon diffusion. Other mechanisms might exist to modulate the luminosity of the TPE, other than the BH accretion rate, such as relativistic jet launching from the BH and shocks due to the relative motion of the star remnant and the tidal streams. A jet might empty a cocoon of low-density material around the TPE, possibly allowing the emission to be less affected by the thick accretion disk or AGN disk. Our results are also subject to a few caveats due to the limitations of our simulations. Future work should address more realistic aspects of TPEs, such as radiation from the hot accretion disk, shocks, binary inspiral from a larger separation, and/or AGN background gas.

Finally, better theoretical understanding of TPEs is highly motivated by the existing observations of abnormal flaring events from AGNs, such as SASSN-15lh and ZTF19aailpwl, that cannot be well explained by AGN variability, or other luminous transients such as TDEs by SMBHs. AGNs are extremely dynamical playgrounds for interacting stars and compact objects. Our results suggest that identifying TPEs among many different ultraluminous transients can be feasible due to their unique accretion signatures and orbital evolution that we find in this work.

Acknowledgments

The authors are grateful to the anonymous referee for comments and suggestions, which helped improve the manuscript. Z.H. acknowledges support from NASA grant 80NSSC22K082. R.P. acknowledges support by NSF award AST-2006839. Y.W. acknowledges support from the Nevada Center for Astrophysics. C.X. acknowledges support from the Department of Astronomy at Columbia University for providing computational resources for this research.

ORCID iDs

Chengcheng Xin https://orcid.org/0000-0003-3106-8182
Zoltán Haiman https://orcid.org/0000-0003-3633-5403
Rosalba Perna https://orcid.org/0000-0002-3635-5677
Yihan Wang https://orcid.org/0000-0002-8614-8721
Taeho Ryu https://orcid.org/0000-0003-2012-5217

References

Artymowicz, P., Lin, D. N. C., & Wampler, E. J. 1993, ApJ, 409, 592
Bartos, I., Kocsis, B., Haiman, Z., & Márka, S. 2017, ApJ, 835, 165
Begelman, M. C. 1979, MNRAS, 187, 237
Cantiello, M., Jermyn, A. S., & Lin, D. N. C. 2021, ApJ, 910, 94
Chen, J.-H., Shen, R.-F., & Liu, S.-F. 2022, ApJ, 947, 32
Coughlin, E. R., Armitage, P. J., Nixon, C., & Begelman, M. C. 2017, MNRAS, 465, 3840
DeLaurentiis, S., Epstein-Martin, M., & Haiman, Z. 2023, MNRAS, 523, 1126
Dempsey, A. M., Li, H., Mishra, B., & Li, S. 2022, ApJ, 940, 155
Dittmann, A. J., Cantiello, M., & Jermyn, A. S. 2021, ApJ, 916, 48
Dittmann, A. J., & Miller, M. C. 2020, MNRAS, 493, 3732
D'Orazio, D. J., & Duffell, P. C. 2021, ApJL, 914, L21
D'Orazio, D. J., Haiman, Z., & MacFadyen, A. 2013, MNRAS, 436, 2997
Eggleton, P. P. 1983, ApJ, 268, 368
Genzel, R., Schodel, R., Ott, T., et al. 2003, ApJ, 594, 812
Goodman, J. 2003, MNRAS, 339, 937
Goodman, J., & Tan, J. C. 2004, ApJ, 608, 108
Hu, H., Inayoshi, K., Haiman, Z., et al. 2022, ApJ, 935, 140
Hwang, H. C., Ting, Y. S., & Zakamska, N. L. 2022, MNRAS, 512, 3383
Iben, I. J., & Tutukov, A. 1984, AJ, 284, 719
Inayoshi, K., Visbal, E., & Haiman, Z. 2020, ARA&A, 58, 27
Jermyn, A. S., Dittmann, A. J., Cantiello, M., & Perna, R. 2021, ApJ, 914, 105
Jiang, Y. F., Stone, J. M., & Davis, S. W. 2014, ApJ, 796, 106
Kaaz, N., Schrøder, S. L., Andrews, J. J., Antoni, A., & Ramirez-Ruiz, E. 2021, ApJ, 944, 44
Kimura, S. S., Murase, K., & Bartos, I. 2021, ApJ, 916, 111
Kıroğlu, F., Lombardi, J. C., Kremer, K., et al. 2022, ApJ, 948, 89
Kitaki, T., Mineshige, S., Ohsuga, K., & Kawashima, T. 2021, PASJ, 73, 450
Kolykhalov, P. I., & Syunyaev, R. A. 1980, SvAL, 6, 357
Kremer, K., Chatterjee, S., Rodriguez, C. L., & Rasio, F. A. 2018, ApJ, 852, 29
Kremer, K., Lombardi, J. C., Lu, W., Piro, A. L., & Rasio, F. A. 2022, ApJ, 933, 203
Kremer, K., Lu, W., Piro, A. L., et al. 2021, ApJ, 911, 104
Lajoie, C. P., & Sills, A. 2011, ApJ, 726, 67
Levin, Y. 2003, arXiv:astro-ph/0307084
Li, J., Dempsey, A. M., Li, H., Lai, D., & Li, S. 2023, ApJL, 944, L42
Li, R., & Lai, D. 2022, MNRAS, 517, 1602
Li, Y.-P., Dempsey, A. M., Li, S., Li, H., & Li, J. 2021, ApJ, 911, 124
Linial, I., & Sari, R. 2017, MNRAS, 469, 2441

Lombardi, J. C., Jr., Proulx, Z. F., Dooley, K. L., et al. 2006, ApJ, 640, 441
Lopez, Martin, J., Batta, A., Ramirez-Ruiz, E., Martinez, I., & Samsing, J. 2019, ApJ, 877, 56
Mackey, A. D., Wilkinson, M. I., Davies, M. B., & Gilmore, G. F. 2007, MNRAS: Letters, 379, 40
Mainetti, D., Lupi, A., Campana, S., et al. 2017, A&A, 600, A124
Meibom, S., & Mathieu, R. D. 2005, ApJ, 620, 970
Metzger, B. D., Stone, N. C., & Gilbaum, S. 2022, ApJ, 926, 101
Muñoz, D. J., Miranda, R., & Lai, D. 2019, ApJ, 871, 84
Nicholl, M., Srivastav, S., Fulton, M. D., et al. 2023, ApJL, 954, L28
Paumard, T., Genzel, R., Martins, F., et al. 2006, in Journal of Physics: Conf. Ser. 54, The Universe under the Microscope—Astrophysics at High Angular Resolution, 54, ed. R. Schoedel et al. (Bristol: IOP Publishing), 199
Paxton, B., Smolec, R., Schwab, J., et al. 2019, ApJS, 243, 10
Perets, H. B., Li, Z., Lombardi, J. C. J., & Milcarek, S. R. J. 2016, ApJ, 823, 113
Perna, R., Lazzati, D., & Cantiello, M. 2021, ApJL, 906, L7
Price, D. J., Wurster, J., Tricco, T. S., et al. 2018, PASA, 35, e031
Rodriguez, C. L., Chatterjee, S., & Rasio, F. A. 2016, PhRvD, 93, 084029
Rowan, C., Boekholt, T., Kocsis, B., & Haiman, Z. 2023a, MNRAS, 524, 2770
Rowan, C., Whitehead, H., Boekholt, T., Kocsis, B., & Haiman, Z. 2023b, arXiv:2309.14433
Ryu, T., Perna, R., Pakmor, R., et al. 2023, MNRAS, 519, 5787
Ryu, T., Perna, R., & Wang, Y.-H. 2022, MNRAS, 516, 2204
Shakura, N. I., & Sunyaev, R. A. 1973, A&A, 24, 337
Siwek, M., Weinberger, R., & Hernquist, L. 2023, MNRAS, 522, 2707
Strader, J., Chomiuk, L., MacCarone, T. J., Miller-Jones, J. C., & Seth, A. C. 2012, Natur, 490, 71
Taam, R. E., & Sandquist, E. L. 2000, ARA&A, 38, 113
Tagawa, H., Haiman, Z., & Kocsis, B. 2020, ApJ, 898, 25
Tagawa, H., Kimura, S. S., Haiman, Z., et al. 2022, ApJ, 927, 41
Van Haaften, L. M., Nelemans, G., Voss, R., Wood, M. A., & Kuijpers, J. 2012, A&A, 537, 104
Wang, Y.-H., Lazzati, D., & Perna, R. 2022, MNRAS, 516, 5935
Wang, Y. H., Perna, R., & Armitage, P. J. 2021, MNRAS, 503, 6005
Wevers, T., Coughlin, E. R., Pasham, D. R., et al. 2022, ApJL, 942, L33
Whitehead, H., Rowan, C., Boekholt, T., & Kocsis, B. 2023, arXiv:2309.11561
Yang, Y., Bartos, I., Fragione, G., et al. 2022, ApJL, 933, L28
Yang, Y., Gayathri, V., Bartos, I., et al. 2020, ApJL, 901, L34
Zalamea, I., Menou, K., & Beloborodov, A. M. 2010, MNRAS, 409, L25
Zrake, J., Tiede, C., MacFadyen, A., & Haiman, Z. 2021, ApJL, 909, L13